Strongly correlated perovskite lithium ion shuttles

Yifei Sun[a,1], Michele Kotiuga[b,1,2], Dawgen Lim[a], Badri Narayanan[c], Mathew Cherukara[d], Zhen Zhang[a], Yongqi Dong[d], Ronghui Kou[d], Cheng-Jun Sun[d], Qiyang Lu[e,f], Iradwikanari Waluyo[g], Adrian Hunt[g], Hidekazu Tanaka[h], Azusa N. Hattori[h], Sampath Gamage[i], Yohannes Abate[i], Vilas G. Pol[j], Hua Zhou[d], Subramanian K. R. S. Sankaranarayanan[k], Bilge Yildiz[e,f,l], Karin M. Rabe[b,2], and Shriram Ramanathan[a]

[a]School of Materials Engineering, Purdue University, West Lafayette, IN 47907; [b]Department of Physics and Astronomy, Rutgers, The State University of New Jersey, Piscataway, NJ 08854; [c]Materials Science Division, Argonne National Laboratory, Argonne, IL 60439; [d]X-Ray Science Division, Advanced Photon Source, Argonne National Laboratory, Argonne, IL 60439; [e]Laboratory for Electrochemical Interfaces, Massachusetts Institute of Technology, Cambridge, MA 02139; [f]Department of Materials Science and Engineering, Massachusetts Institute of Technology, Cambridge, MA 02139; [g]National Synchrotron Light Source II, Brookhaven National Laboratory, Upton, NY 11973; [h]Institute of Scientific and Industrial Research, Osaka University, Osaka 567-0047, Japan; [i]Department of Physics and Astronomy, University of Georgia, Athens, GA 30602; [j]Davidson School of Chemical Engineering, Purdue University, West Lafayette, IN 47907; [k]Center for Nanoscale Materials, Argonne National Laboratory, Argonne, IL 60439; and [l]Department of Nuclear Science and Engineering, Massachusetts Institute of Technology, Cambridge, MA 02139

Contributed by Karin M. Rabe, July 11, 2018 (sent for review March 26, 2018; reviewed by Chris Marianetti and Steven May)

Solid-state ion shuttles are of broad interest in electrochemical devices, nonvolatile memory, neuromorphic computing, and biomimicry utilizing synthetic membranes. Traditional design approaches are primarily based on substitutional doping of dissimilar valent cations in a solid lattice, which has inherent limits on dopant concentration and thereby ionic conductivity. Here, we demonstrate perovskite nickelates as Li-ion shuttles with simultaneous suppression of electronic transport via Mott transition. Electrochemically lithiated $SmNiO_3$ (Li-SNO) contains a large amount of mobile Li^+ located in interstitial sites of the perovskite approaching one dopant ion per unit cell. A significant lattice expansion associated with interstitial doping allows for fast Li^+ conduction with reduced activation energy. We further present a generalization of this approach with results on other rare-earth perovskite nickelates as well as dopants such as Na^+. The results highlight the potential of quantum materials and emergent physics in design of ion conductors.

ionic conductivity | emergent phenomena | Mott transition | neuromorphic | perovskite nickelate

Solid-state ionic shuttles or conductors are of interest in energy storage, voltage-driven ion channels for neuromorphic computing, and various iontronics technologies wherein ionic injection and transport is coupled with electronic band structure modification in complex semiconductors (1, 2). For the case of lithium ions, the ideal conductor should have a large concentration of mobile Li^+ and optimized migration channels with minimal activation energy for diffusion (3). To date, Li^+ conductors make up a diverse set of materials (4–8), among which oxide conductors are prominent (9). For instance, typical oxide-based Li^+ conductor classes include materials similar to lithium and sodium super ionic conductors—LISICON (10) and NASICON (11), $Li_{2.9}PO_{3.3}N_{0.46}$ (LiPON) (12), glass (13), perovskite (14), and Ga-substituted $La_3Zr_2Li_7O_{12}$ (LLZGO) garnet (15). Fundamentally, Li^+ conduction in a perovskite lattice follows the percolation pathway in A-site vacancy and its conductivity is sensitive to the structure and mobile Li^+ concentration (16–18). As an example, A-site deficient lithium lanthanum titanate $[Li_{3x}La_{2/3-x}\square_{1/3-2x}TiO_3\ (0 < x < 0.167)]$ with different amounts of Li^+ substitution, has been investigated. The optimal composition corresponds to $x = 0.11$, that is, $Li_{0.34}La_{0.51}TiO_{2.94}$ (LLTO), which results in room temperature bulk conductivity of 10^{-3} S·cm^{-1} and activation energy of 0.4 eV. Efforts have been devoted to further enhance ionic conductivity of LLTO via heteroatom doping, including B-site substitution by Al^{3+}—$Li_{0.36}La_{0.56}\square_{0.08}Ti_{0.97}Al_{0.03}O_3$ (LLTAO) (19), A-site substitution by Sr^{2+} (19) and Nd^{3+} (20), as well as oxygen-site substitution by fluorine (21). However, the general strategy of heteroatom doping still suffers from fundamental limitations on the extent of Li^+ dopants that can be incorporated substitutionally and are mobile at given temperature (22). Therefore, new approaches to design high performance oxide Li^+ conductors are of great interest.

Here, we report a class of Li-ion shuttles based on emergent electron localization in rare-earth perovskite nickelates. As a representative system, room temperature $SmNiO_3$ (SNO) with perovskite structure (ABO_3) is a narrow-gapped semiconductor with intrinsic conductivity (23). Upon electron filling, the Ni in pristine SNO experiences crossover to Ni^{2+} with a highly localized state (e_g^2) and colossal suppression of electronic conductivity due to electron–electron coulomb interaction (24–26). Instead of cation substitution, the heteroatoms that are electron donors occupy the interstitial sites of host lattice and have weak bonding to coordinated ligands. Recent work has demonstrated the potential of proton-doped correlated nickelate materials as electric field sensors (27). Besides hydrogen, alkaline or alkaline-earth metals such as Li possessing larger ionic radius, can also be regarded as electron donors, which effectively modulate the

Significance

Designing solid-state ion conductors is of broad interest to energy conversion, bioengineering, and information processing. Here, we demonstrate a new class of Li-ion conducting quantum materials in the perovskite family. Rare-earth perovskite nickelate films of the chemical formula $SmNiO_3$ are shown to exhibit high Li-ion conductivity while minimizing their electronic conductivity. This process occurs by electron injection into Ni orbitals when the Li ions are inserted from a reservoir. The mechanism of doping is studied by high-resolution experimental and first-principles theoretical methods to provide evidence for ion shuttling in the lattice and the atomistic pathways. The experiments are then extended to other small ions such as Na^+, demonstrating the generality of the approach.

Author contributions: Y.S. and S.R. designed research; Y.S., M.K., D.L., B.N., M.C., Z.Z., Y.D., R.K., C.-J.S., Q.L., I.W., A.H., H.T., A.N.H., S.G., Y.A., V.G.P., H.Z., S.K.R.S.S., B.Y., K.M.R., and S.R. performed research, for further details see *SI Appendix*; and Y.S. and S.R. wrote the paper with contributions from all authors.

Reviewers: C.M., Columbia University; and S.M., Drexel University.

The authors declare no conflict of interest.

Data deposition: Data associated with the first-principles calculations in this work have been deposited on NOMAD in the dataset Li-SNO_PNAS_2018 (https://repository.nomad-coe.eu/NomadRepository-1.1/doi/result/index.zul?dataset=5841102).

[1]Y.S. and M.K. contributed equally to this work.

[2]To whom correspondence may be addressed. Email: mkotiuga@physics.rutgers.edu or kmrabe@physics.rutgers.edu.

This article contains supporting information online at www.pnas.org/lookup/suppl/doi:10.1073/pnas.1805029115/-/DCSupplemental.

material properties (28). However, their controlled doping, impact on lattice, electrochemical transport behavior, and atomistic migration pathways are as yet unknown and is extremely important to understand given the large difference in ionic radii compared with protons.

We demonstrate a design principle for solid-state Li^+ conductors based on perovskite nickelate thin films (Fig. 1). Pristine room temperature SNO is a semiconductor with a narrow gap, on the order of hundreds of millielectronvolts (Fig. 1*A*). After lithiation via electrochemical poling (Fig. 1*B*), lithium-doped SNO (Li-SNO) is a strongly correlated insulator, with a gap on the order of 3 eV, where the electron localization results in a Mott state where all Ni have valence 2+ (Fig. 1*C*). The doping, electron localization, and reduction of Ni valence (Ni^{3+} to Ni^{2+}) lead to the enlargement of the lattice volume, which elongates the Ni–O bond. The expanded structure allows for a 3D interconnected Li^+ diffusion tunnel. Furthermore, unlike conventional substitutional doping that has structural modulation limits on the extent of dopant accommodation, the concentration of mobile Li^+ in SNO reaches a much higher level, due to the large density of interstitial sites. The interstitial Li^+ is weakly bonded with oxygen ions and exhibits fast conduction behavior across the expanded diffusion bottlenecks. We then present evidence for generalizing the electron-doping principle with other members of the rare-earth nickelate family.

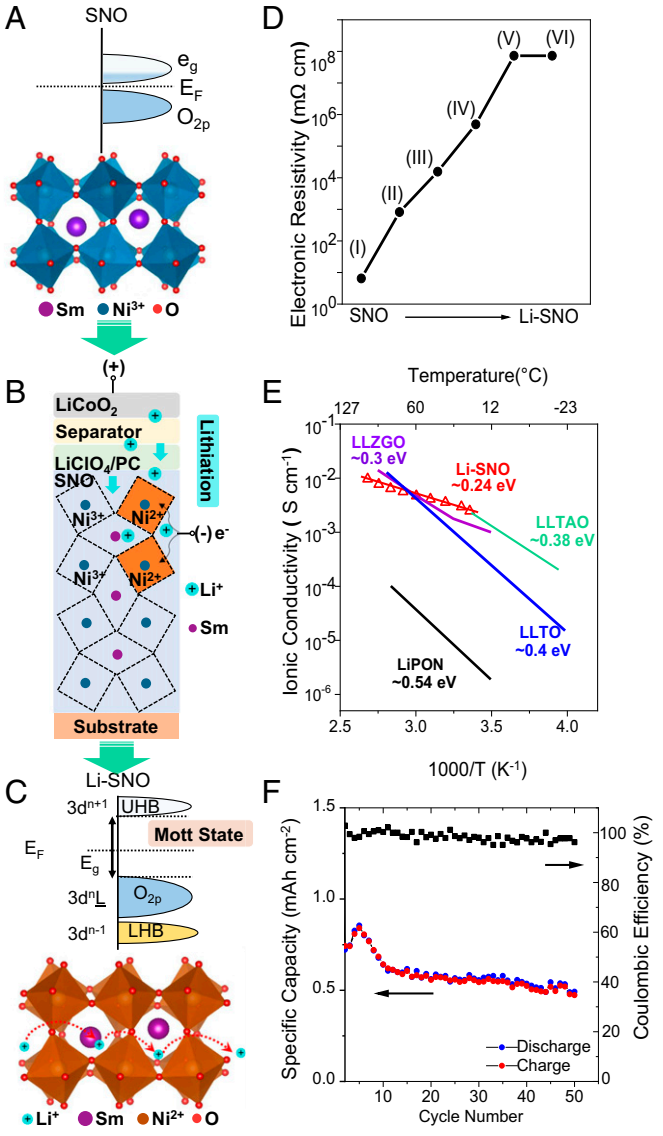

Fig. 1. Lithiated strongly correlated nickelate as ionic conductor. (*A*) Electronic configuration of pristine $SmNiO_3$ (SNO), a narrow-gapped semiconductor at room temperature. (*B*) A self-designed electrochemical cell for lithiation of SNO. (*C*) Electronic configuration of lithiated SNO (Li-SNO). The electron filling leads to large on-site coulomb interaction *U*, suppressing the electronic conduction pathway. Li^+ occupy multiple interstitial sites of the unit cell. The electron localization-induced perovskite lattice expansion facilitates Li^+ interstitial transport, which enables Li-SNO as potential lithium ion conductor. (*D*) Room temperature lithiation induced resistivity evolution of SNO as the function of lithiation time [(I) to (VI) for 0 min, 1 min, 5 min, 30 min, 2 h, and 24 h, respectively]. The Li-SNO becomes transparent and electronically insulating upon 2-h lithiation. (*E*) The Arrhenius ionic conductivity plots of Li-SNO and other representative ionic conductors mentioned in the text. (*F*) Cycling performance of the charge–discharge process of Li-SNO half-cell.

Results

Suppression of electronic transport in SNO upon lithiation can be seen in the evolution of film resistivity (Fig. 1*D*). The pristine SNO shows low resistivity of around 0.6 mΩ·cm at room temperature. A thermal insulator–metal transition point is observed at ∼140 °C, indicating good film quality. Lithiation for 1 min enhances the film resistivity by nearly three orders of magnitude to $\sim 10^3$ mΩ·cm, along with a visual color change. As lithiation proceeds, the film becomes much more transparent and the resistivity continues to increase to $\sim 10^8$ mΩ·cm and then nearly saturates, indicating significant suppression of electronic conduction (denoted as Li-SNO). This saturated low electronic conductivity indicates the Mott state. Direct real-space nanoimaging at terahertz frequencies also highlights this carrier suppression effect. (*SI Appendix*, Fig. S2).

Fig. 1*E* shows the Arrhenius conductivity plots of Li-SNO and other representative oxide Li^+ conductors. Li-SNO has room temperature ionic conductivity of 3.1×10^{-3} S·cm^{-1} with low activation barrier of ∼0.24 eV, comparable to even organic liquid systems. The cycling performance of the lithiation–delithiation process (Fig. 1*F* and *SI Appendix*, Fig. S3*A*) demonstrates an average coulombic efficiency of 96.8%. Upon cycling, the Li-SNO maintained transparency throughout the experiments, indicating that under galvanostatic lithiation, of up to 4.2 V, the material remains stable. These studies demonstrate the shuttling of Li ions across the perovskite lattice under electric fields.

Collective phenomena due to strong electron–electron correlations leads to these striking observations in the perovskite nickelate. In Li-SNO, the transport bottleneck from the flexible tilting of the NiO_6 octahedra controls the interstitial Li^+ diffusion across adjacent hopping sites. The larger Ni^{2+} radius combined with the electron localization effect synergistically increase the Ni–O bond length and result in volume expansion of the perovskite unit cell, which significantly reduces the Li^+ transport barrier.

To show that lithiation does indeed lead to reduction of the Ni sites, we measured X-ray photoelectron spectroscopy (XPS) spectra of Ni ($2p_{3/2}$) peak and Li (1s) peak (*SI Appendix*, Fig. S4). The Ni peak shifts to lower binding energy after lithiation, demonstrating the increase in the fraction of Ni(II) and decrease in the fraction of Ni(III) in Li-SNO. As the lithiation proceeded, the Li_{1s} peak intensity gradually increased, indicating increasing content of Li^+ (Li^+:Ni ∼ 0.86 for fully doped Li-SNO).

To further illustrate the detailed change in the electronic structure upon lithiation, we characterize the films with X-ray absorption near-edge spectroscopy (XANES). In the normalized Ni *K*-edge XANES (Fig. 2*A*), the preedge (feature A) points to the covalence between O_{2p} and Ni_{3d} orbital. The rest of absorption features essentially stem from two different coordination shells, for example, the first shell (in features B, D, E) is formed by octahedral oxygen coordination while the second shell (features C and C′) is due to rare-earth atoms in a

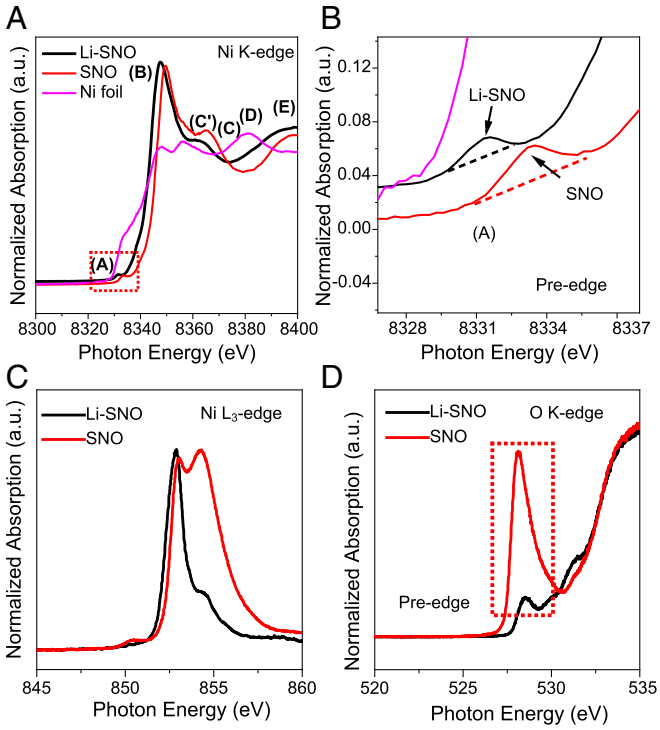

Fig. 2. X-ray absorption of Li-SNO. (*A*) Ex situ normalized Ni *K*-edge, (*B*) preedge of ex situ normalized Ni *K*-edge, (*C*) Ni L_3-edge, and (*D*) O *K*-edge of X-ray absorption near-edge spectroscopy (XANES) characterization of pristine SNO and Li-SNO. As a reference, the spectrum of Ni foil was used for energy calibration.

pseudocubic coordination (29). The intensity of feature A (Fig. 2*B*) significantly decreased after lithiation, indicating the Ni valence decrease. Ni L_3-edge spectra of SNO also shows drastic changes after lithiation with diminished peak at ~855 eV, stressing the transition of Ni^{3+} to Ni^{2+} (Fig. 2*C*) (30). A detailed comparison of preedge area (Ni *K*-edge) clearly shows that the lithiation process decreases the concentration of ligand hole ($3d^8\underline{L}$ in the ground state of Ni, where L denotes a hole state generated in ligand p orbital) by 40% (29). Further study on the O *K*-edge spectra (Fig. 2*D*) indicates a reduced O-projected density of unoccupied states due to lithiation induced electron filling, suggesting the formation of Ni^{2+}. The rest of the holes within O^{2-} could bond with Li^+ and facilitate its transport. The first derivative plot (*SI Appendix*, Fig. S5 *A* and *B*) of the Ni *K*-edge XANES presents a shift of the preedge and absorption edge toward lower energy by 1.65 eV for the 2-h–lithiated sample. Previous studies have shown a slope shift of 1–2 eV/electron charge for Ni-containing oxides with octahedral coordination (31). An effective change in valence of −1 for the Ni ions is seen here. Such lithiation-induced phase transition phenomena can propagate through the film thickness (*SI Appendix*, Fig. S6).

The lithiation of SNO initially leads to the interstitial intercalation of Li^+ and electron localization, which further results in structural distortion. To obtain quantitative information on the lattice parameter evolution of SNO upon lithiation, synchrotron X-ray diffraction (XRD) was performed and the corresponding pattern is shown in Fig. 3*A*. Pristine SNO has a pseudocubic lattice constant of 3.799 Å, which is quite close to that of the $LaAlO_3$ (LAO) substrate (3.790 Å) (32). As seen in curve I of Fig. 3*A*, the SNO exhibits a shoulder [(220) peak, orthorhombic notation] located at $q_z = 3.29$ $Å^{-1}$ close to LAO (002) peak (pseudocubic notation). Lithiation induces the appearance of peaks at $q_z = 2.98$ $Å^{-1}$ corresponding to ~9.1% out-of-plane lattice dilatation (curve II in Fig. 3*A*). Noticeably, the XRD peak of SNO parent phase becomes narrower with Li intercalation, which may be attributed to electrochemical crystallization, which is sometimes referred to as "cold annealing" process (33, 34). Two-dimensional reciprocal space mapping (RSM) around the pseudocubic (002) reflections of pristine SNO and Li-SNO (Fig. 3 *B* and *C*) further confirm lattice expansion of ~9% in Li-SNO. The lithiation induced thin film lattice expansion was further seen in synchrotron X-ray reflectivity (XRR) (Fig. 3*D*). Compared with the pristine state, a significantly decreased oscillation period of Li-SNO can be observed, due to the increase of film thickness. This significant lattice expansion due to NiO_6 octahedral distortion can then be correlated to the reduced diffusion activation energy (35).

It further can be seen in the first derivative plot of the Ni *K*-edge XANES spectra (*SI Appendix*, Fig. S5*C*) that the energy separation between A and B feature is ~16.45 eV for pristine SNO, which is larger than that of Li-SNO (~15.35 eV). The significant change in energy splitting suggests that lithiation enhances the lattice distortion and increases the Ni–O bond length. The fitted Fourier-transformed extended X-ray absorption fine structure (EXAFS) spectra (Fig. 3*E* and *SI Appendix*, Fig. S7) gives a local picture of the Ni coordination shells. The first peak (A) at ~1.5 Å is from the Ni–O coordination shell, and the feature at 2.6 Å stems from the Ni–Sm shells. Lithiation not only leads to the decrease of the Ni–O peak intensity but also shifts

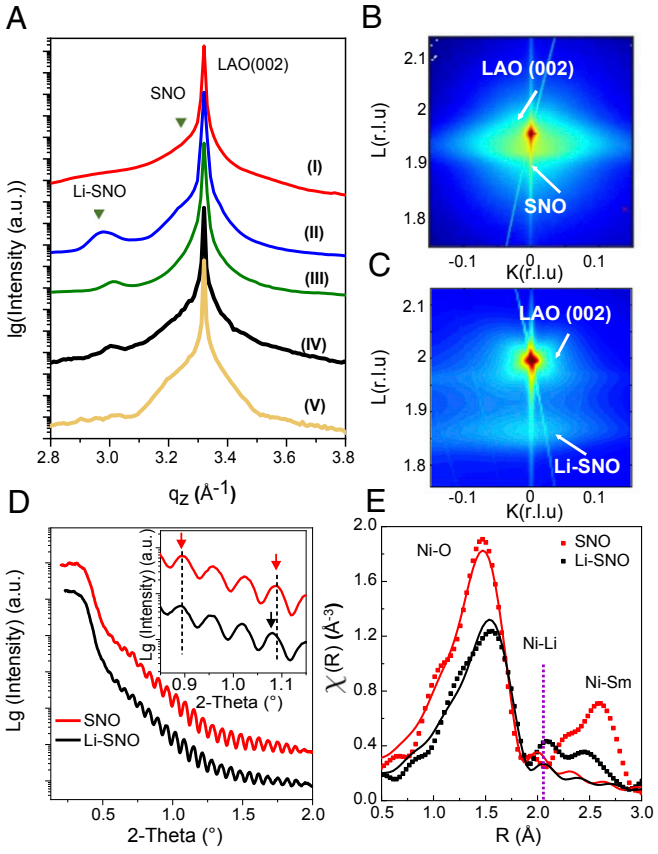

Fig. 3. Structural configuration of Li-SNO. (*A*) In situ synchrotron X-ray diffraction (XRD) pattern of SNO upon charge–discharge cycles. (I) Pristine SNO, (II) Li-SNO, (III) 1 cycle, (IV) 20 cycles, and (V) 50 cycles. (*B* and *C*) Two-dimensional reciprocal space mapping (RSM) around the pseudocubic (002) reflection of (*B*) pristine SNO and (*C*) Li-SNO. (*D*) Synchrotron X-ray reflectivity (XRR) pattern comparison of SNO and Li-SNO. (*E*) Fourier transform of the Ni *K*-edge EXAFS (dots) and the fitting (lines) of SNO and Li-SNO.

the peak position toward larger radius, which is in part due to the larger Ni(II) ions in SNO (36). The fitting results demonstrate that the Ni–O bond length expands by 0.08 Å due to the Li doping (from 1.95 to 2.03 Å). Noticeably, a distinct feature around 2.2 Å was found in Li-SNO, which we ascribed to an additional Ni–Li shell between Ni–O and Ni–Sm, further strengthening our hypothesis that Li^+ occupies interstitial sites. In situ synchrotron XRD experiments were performed to detect the structural evolution during cycling (Fig. 3*A*). The diffraction peak at $q_z = 2.98$ $Å^{-1}$ shifts to 3.03 $Å^{-1}$ (curve III in Fig. 3*A*). Multiple cycles make the SNO thin film disordered (weak Laue fringes between $q_z = 2.8$–3.1 $Å^{-1}$ in curves IV and V in Fig. 3*A*); the high electronic resistance of Li-SNO, however, is still maintained.

First-principles density functional theory (DFT) calculations are carried out on pristine SNO in a monoclinic cell with no breathing distortion, as such a distortion is not observed in room temperature SNO. As lithium is added to SNO, its valence electron localizes on a Ni site, thus converting it to Ni^{2+}. The localization of the electron on the Ni^{3+} is clearly observed as the local magnetic moment increases from 0.8 μ_B (Ni^{3+}) to 1.6 μ_B (Ni^{2+}). The Li valence electron occupies a previously unoccupied Ni–O state and does not introduce a lithium state near the Fermi energy. In fact, once a Ni site is converted to Ni^{2+}, the remaining unoccupied e_g states are pushed up in energy relative to the occupied e_g states due to electron–electron correlations, leading to a much larger band gap once all of the nickel are converted to Ni^{2+} (Fig. 4*A*).

Structural optimization calculations using DFT show that at a concentration of 1:4 Li^+:Ni the lowest-energy intercalated Li^+ ion is tetrahedrally coordinated by four oxygens from two adjacent corner-sharing NiO_6 octahedra. These octahedra are canted toward each other with an out-of-phase tilt angle between them such that the LiO_4 tetrahedron is face-sharing with one NiO_6 octahedron and edge-sharing with the other (Fig. 4*B*). For details, see *SI Appendix*, Fig. S8 *J–M*. The added Li valence electron causes an increase in the volume of the NiO_6 octahedron that contains a Ni^{2+} ion, which is not necessarily the closest Ni to the intercalated Li^+, as the localized electron need not sit on one of the adjacent NiO_6 octahedra. At a concentration of 1:1 Li^+:Ni, the lowest energy structure has intercalated Li^+ tetrahedrally coordinated in the face–edge sharing configuration described above as well as Li^+ between two octahedra canted toward each other with an in-phase tilt angle between them such that the LiO_4 tetrahedra is edge-sharing with both NiO_6 octahedra (*SI Appendix*, Fig. S8 *G–I*). Informed by the experimental characterization and the molecular dynamics calculations presented below, however, it seems that this structure is kinetically inaccessible. Restricting our attention to geometries where the Li^+ remains in the face–edge sharing tetrahedra, the calculated overall volume expansion for 1 Li/Ni is ~10%, when the cell is allowed to expand in the (110) direction matching the epitaxial condition of the experimental film, consistent with diffraction data (Fig. 4*C*). For the series of geometries shown in Fig. 4*B*, the average Ni–O bond length increases 0.07 Å (from 2.002 Å in SNO to 2.074 Å in Li-SNO), the coordination number decreases by around 1 (6 to 5), and the average Ni–Li bond length is ~2.1 Å, in good agreement with the EXAFS results (*SI Appendix*, Table S1). The lattice expansion mechanism associated with donor doping from Li described here is similar to the lattice expansion caused by donor doping by oxygen vacancies in oxides (37). The larger the extent of localization of the electron on the redox active metal cation, the larger the expansion in the structure (38).

Ab initio molecular dynamics (AIMD) and DFT calculations were performed to understand Li migration pathways through the SNO lattice and the associated barriers. During a typical AIMD run at a modest temperature of 300 K, we observe

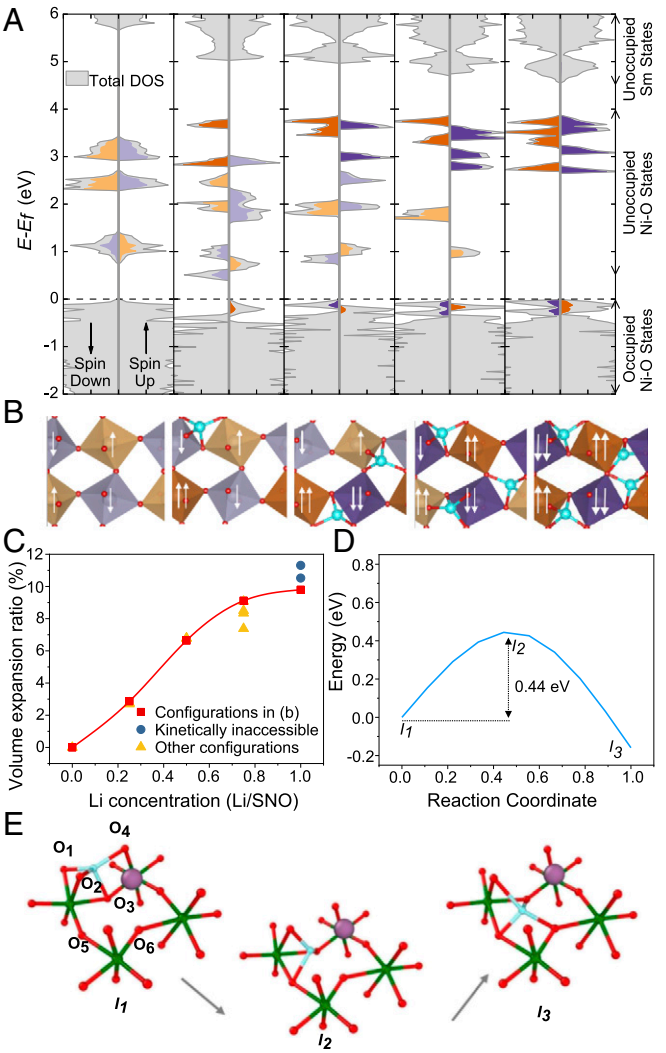

Fig. 4. First-principles simulation of Li-SNO and interstitial diffusion. (*A*) Total density of states of SNO with 0–1 intercalated Li/SNO (gray). The projected DOS (PDOS) of the unoccupied Ni e_g states are shown in color. The lighter hues indicate e_g states of Ni^{3+} and the darker hues of Ni^{2+} including the newly occupied e_g states due to the localization of the added electron from the intercalated lithium below the Fermi energy. The character of the localized electrons is primarily oxygen, consistent with the reduction of the O–K preedge seen in the XANES characterization. (*B*) The $\sqrt{2}\times\sqrt{2}\times 2$ SNO supercells with 0–1 Li/SNO showing the tetrahedral coordination of the Li. The arrows indicate the occupancy of the Ni e_g states and the color of the octahedra correspond to the PDOS above. (*C*) The lattice volume evolution as a function of Li/SNO concentration while allowing the (110) direction to relax. The red points correspond to the geometries shown in *B*, the blue points to kinetically inaccessible configurations, and the yellow to geometries with different lithium positions occupied (*SI Appendix*, Fig. S8). (*D* and *E*) Atomic-scale pathways and the associated barriers for Li migration in SNO lattice calculated using CI-NEB calculations within the framework of DFT+*U*. The potential energy along the most preferred pathway is shown for Li migration between two adjacent O-tetrahedral sites, when the neighboring tetrahedral sites are either above/below the ring formed by Ni atoms and the shared O-corners of four adjacent NiO_6 octahedra (as shown in atomic plots).

frequent Li hopping from one tetrahedral site to a nearby one. Climbing-image nudged elastic band (CI-NEB) calculations within the framework of DFT+*U* for an isolated Li hop in an unstrained SNO lattice reveal an energetic barrier of ~0.44 eV (Fig. 4*D*). The optimal diffusion pathway involves migration of Li between two tetrahedral sites above the ring formed by the

four Ni, and four shared O corners. This hopping is facilitated by the rotation of a Li–O bond about two corner-shared NiO_6 octahedra, and consequent distortion of the initial LiO_4 tetrahedron (Fig. 4*E*, *SI Appendix*, Fig. S9, and Movie S1). Recent ab initio modeling suggests concerted migration of multiple Li ions can proceed with energy barriers that are much lower than isolated Li hops, owing to strong ion–ion interactions at high Li concentrations (39). Future studies therefore may focus on exploring the effects of concentration dependence of ion diffusivity coupled with strain.

The expanded Ni–O bond lengths facilitating faster Li mobility in this system is akin to the larger mobility and reduced migration barriers of oxygen atoms in tensile strained oxides (40, 41). Experimental studies of Na^+ intercalation into SNO (*SI Appendix*, Fig. S10) as well as Li^+ doping experiments in related rare-earth perovskite nickelate systems [$EuNiO_3$ (ENO) and $NdNiO_3$ (NNO)] further suggest the generality of the electrochemical poling strategy to design ion shuttles in strongly correlated oxides (*SI Appendix*, Fig. S11).

Conclusions

We demonstrate that cations such as Li^+, Na^+ can be reversibly incorporated into perovskite nickelate lattices under voltage bias in electrochemical cells. Strain due to ion incorporation in interstitial sites enables rapid diffusion with reduced activation barriers. The electron doping from intercalated Li, resulting in Ni^{2+}, suppresses electronic conduction and enables selective ionic transport with tunable resistance states.

Methods

Growth of Thin Films. SNO thin films of various thickness (80–200 nm) were grown on LAO substrate using magnetron sputtering combined with post-annealing in high-pressure high-purity oxygen atmosphere. The deposition condition is 40/10 sccm Ar/O_2 mixture at total pressure of 5 mtorr from two metallic Ni (DC) and Sm (RF) targets (*SI Appendix*, Fig. S1*A*). The stoichiometry of Sm/Ni was confirmed by energy-dispersive X-ray spectroscopy (EDS) equipped with field emission–scanning electron microscopy (FE-SEM). The as-deposited samples were annealed in a high-pressure vessel under 1,500 psi of pure O_2 (99.99%) at 500 °C for 24 h in a tube furnace. Due to the metastable nature of samarium nickelate perovskite phase, such high-pressure annealing is necessary, which may lead to weaker XRD peaks as film thickness increases due to the slower kinetics required to propagate texture throughout the film thickness. Film thickness is ∼100 nm prepared for the characterization studies (*SI Appendix*, Fig. S1 *B–D*). Details of the growth of the $EuNiO_3$ and $NdNiO_3$ thin films can be found in *SI Appendix*.

Lithium Doping Process in SNO. One molar $LiClO_4$ (Sigma Aldrich) is dissolved in polyethylene carbonate (PC) in an argon-filled glovebox with oxygen and moisture levels at <0.5 ppm. A drop of 1 M $LiClO_4$ | PC was dispersed on SNO | LAO thin film. A commercial $LiCoO_2$ supported on current collector Al foil was used as lithium source for lithiation. As separator, a piece of polymer membrane (Celgard 2500) is placed underneath the $LiCoO_2$ | Al foil, avoiding the direct contact to SNO | LAO thin film. A positive bias is applied to the $LiCoO_2$ | Al foil, and thin film serves as the ground electrode for lithiation process.

Conductivity Measurements. The as-annealed and lithiated thin films were first cleaned with toluene/acetone/isopropanol solutions and dried with argon gas. Two Pt bars (1 cm × 1 mm × 100 nm, 5-mm gap) were deposited onto film surface using e-beam evaporator at room temperature, serving as the top contacts. The resistivity of thin films were measured using a two point method on a Keithley 2635A instrument in laboratory air environment at room temperature. The in-plane ionic conductivity of thin film was carried out using AC electrochemical impedance spectroscopy (EIS) at frequencies ranging from 1 MHz to 1 Hz on a Solartron 1260/1287 instrument. As blocking electrodes, an array of platinum bars was deposited onto the films using a metal shadow mask in CHA e-beam evaporator instrument. The distance between two electrodes (L) is much larger than the thickness (H) of thin film to prevent the current constriction effect (42). A represents the conducting area. The ionic conductivity (S) of thin film can be calculated based on the following: $S = 1/R^*(L/A)$. The R value can be obtained via fitting the EIS curve.

Electrochemical Test for Film Cycleability. A closed sandwich half-cell structure consisting of Li | 1 M $LiPF_6$ in EC:DEC (1:1) (Sigma-Aldrich) | polymer membrane (Celgard 2500) | Li-SNO (200 nm) | Pt | LAO, where bar-shaped (2 × 10 mm) platinum electrode (100 nm in thickness) is deposited on LAO using an e-beam instrument (CHA) at room temperature. Then the SNO film was deposited next. Commercial Li metal disk served as another electrode. Galvanostatic charge discharge is then conducted on the cell with a current density of 5 $\mu A \cdot cm^{-2}$ and a cutoff voltage from 0.5 to 4.2 V for a total cycle of 50 cycles. All tests were performed in an argon-filled glovebox with oxygen and moisture levels at <0.5 ppm. Typical cycle times were for 20 min.

XPS. The XPS characterization was conducted on a Kratos X-ray photoelectron spectrometer equipped with nonmonochromatic dual anode X-ray gun with Al Kα (1,486.6 eV). The spectra is calibrated with C_{1s} peak at 286.4 eV.

Terahertz Time-Domain Nanospectroscopy. Terahertz time-domain nanospectroscopy (THz-TDNS) was employed to assess the change in carrier density that accompanies the Mott transition of SNO. The THz-TDNS is based on scattering-type scanning near-field microscope (s-SNOM) coupled with 1,550-nm fiber laser and InGaAs THz emitter and detector.

Surface Morphology Measurements. The SEM images were collected on FEI XL40 FE-SEM equipped with EDS detector.

Synchrotron X-Ray Measurements. Synchrotron XRR and XRD of the SNO samples were conducted at an insertion device beamline, using X-ray energy of 20 keV at sector of 12ID-D and 33-ID-C at the Advanced Photon Source (APS) in Argonne National Laboratory.

X-Ray Absorption Spectroscopy. The Ni K-edge X-ray absorption spectra (XAS) were performed using linear polarized X-rays at the undulator beamline 20-ID-C of the APS, Argonne National Laboratory. The Si (111) monochromator with resolution $\delta E/E = 1.3 \times 10^{-4}$ was used. The spectra were collected in fluorescence mode using a 12-element Ge solid-state detector. Ni metal foil placed to intercept a scattered beam was used as an online check of the monochromator energy calibration.

Ni $L_{2,3}$-edge and O K-edge XAS were collected by using both total electron yield through drain current measurements and partial fluorescence yield (PFY) modes at the IOS (23-ID-2) beamline of National Synchrotron Light Source II, Brookhaven National Laboratory. PFY spectra were collected using a Vortex silicon drift detector. All of the XAS measurements were performed at room temperature in an ultrahigh-vacuum chamber (base pressure, $\sim 10^{-9}$ torr). A more detailed description of the beamline and end station can be found elsewhere (43). All of the hard X-ray absorption spectra were analyzed by using the Athena and Artemis programs (44, 45).

Ab Initio Calculations. Both the first-principles–based DFT calculations and the AIMD simulations are performed in the framework of DFT+U within the generalized gradient approximation using the projector-augmented wave formalism (46) as implemented in Vienna Ab initio Simulation Package (VASP) (47, 48). We treat the exchange correlation using Perdew–Burke–Ernzerhof functional (49), with the pseudopotentials: Sm_3 (valence, $5s^25p^26s^24f^1$), Ni_pv (valence, $3p^64s^23d^8$), and O (valence, $2s^22p^4$) supplied by VASP, the rotationally invariant form of DFT+U of Liechtenstein et al. (50) using $U = 4.6$ eV and $J = 0.6$ eV, and a plane-wave energy cutoff of 520 eV. All electronic structure calculations are carried out with the tetrahedron method with Blöchl corrections (51), a 6 × 6 × 4 Monkhorst-Pack k-point mesh for the $\sqrt{2} \times \sqrt{2} \times 2$ supercell (20 atoms) with space group $P2_1/n$. When simulating Li-SNO, neutral lithium atoms are added. See *SI Appendix* for further details on the structure determination and the addition of lithium. The computational supercell of the AIMD simulations consists of 4 unit cells (2 × 2 × 1 repetitions of the unit cell; 80 atoms) of monoclinic SNO with space group $P2_1/n$. Periodic boundary conditions are employed along all of the directions and the Brillouin zone is sampled at the Γ-point alone. In these simulations, the atomic positions, cell volume, and the cell shape are all allowed to vary via the Parrinello–Rahman scheme (52); constant temperature conditions are maintained using a Langevin thermostat (53). To compute the barriers associated with Li migration in SNO lattice, we performed CI-NEB (54, 55) calculations for various representative pathways using the same supercell and level of theory as the AIMD simulations. For further details of the thermalization and the addition of lithium, see *SI Appendix*.

ACKNOWLEDGMENTS. We acknowledge National Science Foundation Grant 1609898 and Air Force Office of Scientific Research Grant FA9550-16-1-0159 for support. M.K. and K.M.R. acknowledge support from Office of Naval Research Grant N00014-17-1-2770. D.L. and V.G.P. acknowledge support from Office of Naval Research Grant N00014-18-1-2397. This research used resources of the Argonne Leadership Computing Facility, which is a US Department of Energy (DOE) Office of Science User Facility supported under Contract DE-AC02-06CH11357. Use of the Center for Nanoscale Materials, an Office of Science User Facility, was supported by the US Department of Energy, Office of Science, Office of Basic Energy Sciences, under Contract DE-AC02-06CH11357. This research used resources of the National Energy Research Scientific Computing Center, a DOE Office of Science User Facility supported by the Office of Science of the US DOE under Contract DE-AC02-05CH11231. Z.Z. acknowledges support from Army Research Office Grant W911NF-16-1-0042. This research used resources of the APS, an Office of Science User Facility operated for the US DOE Office of Science by Argonne National Laboratory, and was supported by the US DOE under Contract DE-AC02-06CH11357, and the Canadian Light Source and its funding partners. Q.L. and B.Y. acknowledge funding support from the Massachusetts Institute of Technology Materials Research Science and Engineering Center (MRSEC) through the MRSEC Program of the National Science Foundation under Award DMR-1419807. This research used resources 23-ID-2 beamline of the National Synchrotron Light Source II, a US DOE Office of Science User Facility operated for the DOE Office of Science by Brookhaven National Laboratory under Contract DE-SC0012704. H.T. and A.H. acknowledge Japan Society for the Promotion of Science KAKENHI Grant 15KK0236. S.G. acknowledges support provided by National Science Foundation Grant 1553251. The work of Y.A. was supported by the Air Force Office of Scientific Research Grant FA9559-16-1-0172.

1. Bisri SZ, Shimizu S, Nakano M, Iwasa Y (2017) Endeavor of iontronics: From fundamentals to applications of ion-controlled electronics. *Adv Mater* 29:1607054.
2. Krick AL, May SJ (2017) Evidence for oxygen vacancy manipulation in $La_{1/3}Sr_{2/3}FeO_{3\text{-delta}}$ thin films via voltage controlled solid-state ionic gating. *APL Mater* 5:042504.
3. Bachman JC, et al. (2016) Inorganic solid-state electrolytes for lithium batteries: Mechanisms and properties governing ion conduction. *Chem Rev* 116:140–162.
4. Seino Y, Ota T, Takada K, Hayashi A, Tatsumisago M (2014) A sulphide lithium super ion conductor is superior to liquid ion conductors for use in rechargeable batteries. *Energy Environ Sci* 7:627–631.
5. Kato Y, et al. (2016) High-power all-solid-state batteries using sulfide superionic conductors. *Nat Energy* 1:16030.
6. Rao RP, Adams S (2011) Studies of lithium argyrodite solid electrolytes for all-solid-state batteries. *physica status solidi (a)* 208:1804–1807.
7. Yamane H, Kikkawa S, Koizumi M (1987) Preparation of lithium silicon nitrides and their lithium ion conductivity. *Solid State Ion* 25:183–191.
8. Nazri G (1989) Preparation, structure and ionic conductivity of lithium phosphide. *Solid State Ion* 34:97–102.
9. Ren YY, et al. (2015) Oxide electrolytes for lithium batteries. *J Am Ceram Soc* 98: 3603–3623.
10. Rodger AR, Kuwano J, West AR (1985) Li^+ ion conducting γ solid solutions in the systems Li_4XO_4-Li_3YO_4: X=Si, Ge, Ti; Y=P, as, V; Li_4XO_4-$LiZO_2$: Z=Al, Ga, Cr and Li_4GeO_4-Li_2CaGeO_4. *Solid State Ion* 15:185–198.
11. Aono H, Sugimoto E, Sadaoka Y, Imanaka N, Adachi G (1990) Ionic-conductivity of solid electrolyte based on lithium titanium phosphate. *J Electrochem Soc* 137: 1023–1027.
12. Yu X, Bates JB, Jellison GE, Hart FX (1997) A stable thin-film lithium electrolyte: lithium phosphorus oxynitride. *J Electrochem Soc* 144:524–532.
13. Glass AM, Nassau K, Negran TJ (1978) Ionic conductivity of quenched alkali niobate and tantalate glasses. *J Appl Phys* 49:4808–4811.
14. Inaguma Y, et al. (1993) High ionic conductivity in lithium lanthanum titanate. *Solid State Commun* 86:689–693.
15. Bernuy-Lopez C, et al. (2014) Atmosphere controlled processing of Ga-substituted garnets for high Li-Ion conductivity ceramics. *Chem Mater* 26:3610–3617.
16. Alonso JA, et al. (2000) On the location of Li^+ cations in the fast Li-cation conductor $La_{0.5}Li_{0.5}TiO_3$ perovskite. *Angew Chem Int Ed Engl* 39:619–621.
17. Harada Y, Hirakoso Y, Kawai H, Kuwano J (1999) Order–disorder of the A-site ions and lithium ion conductivity in the perovskite solid solution $La_{0.67-x}Li3_xTiO_3$ ($x = 0.11$). *Solid State Ion* 121:245–251.
18. Harada Y, Ishigaki T, Kawai H, Kuwano J (1998) Lithium ion conductivity of polycrystalline perovskite $La_{0.67-x}Li3_xTiO_3$ with ordered and disordered arrangements of the A-site ions. *Solid State Ion* 108:407–413.
19. Morata-Orrantia A, García-Martín S, Alario-Franco MÁ (2003) Optimization of lithium conductivity in La/Li titanates. *Chem Mater* 15:3991–3995.
20. Teranishi T, Yamamoto M, Hayashi H, Kishimoto A (2013) Lithium ion conductivity of Nd-doped (Li, La)TiO_3 ceramics. *Solid State Ion* 243:18–21.
21. Okumura T, et al. (2009) Improvement of Li-ion conductivity in A-site disordering lithium-lanthanum-titanate perovskite oxides by adding LiF in synthesis. *J Power Sources* 189:536–538.
22. Stramare S, Thangadurai V, Weppner W (2003) Lithium lanthanum titanates: A review. *Chem Mater* 15:3974–3990.
23. Jaramillo R, Ha SD, Silevitch DM, Ramanathan S (2014) Origins of bad-metal conductivity and the insulator–metal transition in the rare-earth nickelates. *Nat Phys* 10: 304–307.
24. Shi J, Zhou Y, Ramanathan S (2014) Colossal resistance switching and band gap modulation in a perovskite nickelate by electron doping. *Nat Commun* 5:4860.
25. Inaguma Y, Chen L, Itoh M, Nakamura T (1994) Candidate compounds with perovskite structure for high lithium ionic conductivity. *Solid State Ion* 70-71:196–202.
26. Shan YJ, Inaguma Y, Itoh M (1995) The effect of electrostatic potentials on lithium insertion for perovskite oxides. *Solid State Ion* 79:245–251.
27. Zhang Z, et al. (2018) Perovskite nickelates as electric-field sensors in salt water. *Nature* 553:68–72.
28. Li Z, et al. (2016) Correlated perovskites as a new platform for super-broadband-tunable photonics. *Adv Mater* 28:9117–9125.
29. García J, Blasco J, Proietti MG, Benfatto M (1995) Analysis of the x-ray-absorption near-edge-structure spectra of $La_{1-x}Nd_xNiO_3$ and $LaNi_{1-x}Fe_xO_3$ perovskites at the nickel *K* edge. *Phys Rev B Condens Matter* 52:15823–15828.
30. Hu Z, et al. (2000) Hole distribution between the Ni 3*d* and O 2*p* orbitals in $Nd_{2-x}Sr_xNiO_{4-\delta}$. *Phys Rev B Condens Matter Mater Phys* 61:3739–3744.
31. Medarde M, et al. (2009) Charge disproportionation in $RNiO_3$ perovskites (R = rare earth) from high-resolution x-ray absorption spectroscopy. *Phys Rev B Condens Matter Mater Phys* 80:245105.
32. Torriss B, Margot J, Chaker M (2017) Metal-insulator transition of strained $SmNiO_3$ thin films: Structural, electrical and optical properties. *Sci Rep* 7:40915.
33. Dahlin AB, Sannomiya T, Zahn R, Sotiriou GA, Vörös J (2011) Electrochemical crystallization of plasmonic nanostructures. *Nano Lett* 11:1337–1343.
34. Gao Q, et al. (2014) Direct evidence of lithium-induced atomic ordering in amorphous TiO_2 nanotubes. *Chem Mater* 26:1660–1669.
35. Li X, Benedek NA (2015) Enhancement of ionic transport in complex oxides through soft lattice modes and epitaxial strain. *Chem Mater* 27:2647–2652.
36. Massa NE, et al. (2015) Temperature and high-pressure dependent x-ray absorption of $SmNiO_3$ at the Ni K and Sm L_3 edges. *Mater Res Express* 2:126301.
37. Marrocchelli D, Bishop SR, Tuller HL, Yildiz B (2012) Understanding chemical expansion in non-stoichiometric oxides: Ceria and zirconia case studies. *Adv Funct Mater* 22: 1958–1965.
38. Marrocchelli D, Bishop SR, Tuller HL, Watson GW, Yildiz B (2012) Charge localization increases chemical expansion in cerium-based oxides. *Phys Chem Chem Phys* 14: 12070–12074.
39. He X, Zhu Y, Mo Y (2017) Origin of fast ion diffusion in super-ionic conductors. *Nat Commun* 8:15893.
40. Kushima A, Yildiz B (2010) Oxygen ion diffusivity in strained yttria stabilized zirconia: Where is the fastest strain? *J Mater Chem* 20:4809–4819.
41. Yildiz B (2014) "Stretching" the energy landscape of oxides—effects on electrocatalysis and diffusion. *MRS Bull* 39:147–156.
42. Hertz JL, Tuller HL (2007) Measurement and finite element modeling of triple phase boundary-related current constriction in YSZ. *Solid State Ion* 178:915–923.
43. Palomino RM, et al. (2017) New in-situ and operando facilities for catalysis science at NSLS-II: The deployment of real-time, chemical, and structure-sensitive X-ray probes. *Synchrotron Radiat News* 30:30–37.
44. Ravel B (2001) ATOMS: Crystallography for the X-ray absorption spectroscopist. *J Synchrotron Radiat* 8:314–316.
45. Ravel B, Newville M (2005) ATHENA, ARTEMIS, HEPHAESTUS: Data analysis for X-ray absorption spectroscopy using IFEFFIT. *J Synchrotron Radiat* 12:537–541.
46. Blöchl PE (1994) Projector augmented-wave method. *Phys Rev B Condens Matter* 50: 17953–17979.
47. Kresse G, Furthmüller J (1996) Efficient iterative schemes for ab initio total-energy calculations using a plane-wave basis set. *Phys Rev B Condens Matter* 54:11169–11186.
48. Kresse G, Joubert D (1999) From ultrasoft pseudopotentials to the projector augmented-wave method. *Phys Rev B Condens Matter Mater Phys* 59:1758–1775.
49. Perdew JP, Burke K, Ernzerhof M (1997) Generalized gradient approximation made simple. *Phys Rev Lett* 78:1396.
50. Liechtenstein AI, Anisimov VI, Zaanen J (1995) Density-functional theory and strong interactions: Orbital ordering in Mott-Hubbard insulators. *Phys Rev B Condens Matter* 52:R5467–R5470.
51. Blöchl PE, Jepsen O, Andersen OK (1994) Improved tetrahedron method for Brillouin-zone integrations. *Phys Rev B Condens Matter* 49:16223–16233.
52. Parrinello M, Rahman A (1981) Polymorphic transitions in single-crystals—a new molecular-dynamic method. *J Appl Phys* 52:7182–7190.
53. Tildesley MPADJ (1987) *Computer Simulation of Liquids* (Oxford Univ Press/Clarendon, Oxford).
54. Henkelman G, Uberuaga BP, Jonsson H (2000) A climbing image nudged elastic band method for finding saddle points and minimum energy paths. *J Chem Phys* 113: 9901–9904.
55. Henkelman G, Jonsson H (2000) Improved tangent estimate in the nudged elastic band method for finding minimum energy paths and saddle points. *J Chem Phys* 113: 9978–9985.